CrossMark

J. Fluid Mech. (2017), *vol.* 827, *pp.* 457–483. © Cambridge University Press 2017
doi:10.1017/jfm.2017.499

Mineral dissolution and wormholing from a pore-scale perspective

Cyprien Soulaine[1],†, Sophie Roman[1], Anthony Kovscek[1] and Hamdi A. Tchelepi[1]

[1]Department of Energy Resources Engineering, Stanford University, Stanford, CA 95305, USA

(Received 13 January 2017; revised 23 May 2017; accepted 17 July 2017;
first published online 24 August 2017)

A micro-continuum approach is proposed to simulate the dissolution of solid minerals at the pore scale under single-phase flow conditions. The approach employs a Darcy–Brinkman–Stokes formulation and locally averaged conservation laws combined with immersed boundary conditions for the chemical reaction at the solid surface. The methodology compares well with the arbitrary-Lagrangian–Eulerian technique. The simulation framework is validated using an experimental microfluidic device to image the dissolution of a single calcite crystal. The evolution of the calcite crystal during the acidizing process is analysed and related to the flow conditions. Macroscopic laws for the dissolution rate are proposed by upscaling the pore-scale simulations. Finally, the emergence of wormholes during the injection of acid in a two-dimensional domain of calcite grains is discussed based on pore-scale simulations.

Key words: low-Reynolds-number flows, nonlinear instability, porous media

1. Introduction

Dissolution of solid minerals in porous media is important in many subsurface transport processes. Application areas include subsurface hydrology, reservoir engineering and CO_2 sequestration. For example, a common practice in petroleum engineering involves the injection of acid, usually hydrochloric acid for carbonate formations, to enhance the conductivity around the wellbore by dissolution and creation of ramified wormholes (Williams, Gidley & Schechter 1979). Another example concerns the sequestration of CO_2 in deep saline aquifers. The injected supercritical CO_2 exists as a separate fluid phase that is immiscible with the resident brine. Complex interfacial (fluid–fluid and fluid–solid) dynamics that depends strongly on the wettability of the mineral surface can lead to the trapping of CO_2 ganglia in the pore space. CO_2 from the supercritical phase dissolves in the aqueous (brine) phase to form carbonic acid, which lowers the pH of the brine as the carbonic acid dissociates into bicarbonate ions (Steefel, Molins & Trebotich 2013; Cohen & Rothman 2015). The acid ions are then transported by advection and diffusion to the mineral surface where the dissolution and precipitation of the minerals may occur (Molins *et al.* 2014). Calcite (a type of carbonate mineral) dissolution is one of the most important dissolution reactions that occurs during sequestration (Rathnaweera, Ranjith & Perera 2016). These dynamic processes associated with the injection

† Email address for correspondence: csoulain@stanford.edu

https://doi.org/10.1017/jfm.2017.499 Published online by Cambridge University Press

and sequestration of CO_2 into deep saline aquifers can produce significant changes in the pore space leading to significant changes in macroscopic properties, such as permeability and porosity (Rathnaweera *et al.* 2016). Accurate and efficient modelling of dissolution processes in natural porous media is important to assess the long-term integrity of the caprock in many settings, and to improve engineering practice for acid stimulation of carbonate formations.

Dissolution patterns take different forms according to the flow conditions and mineral properties. For example, at small injection rates, the characteristic time scale for reaction can be quite small compared with that of acid transport; in this case, the acid gets consumed as it invades the porous formation around the wellbore. The propagation of the acid into the formation is then limited, which leads to a facial – or compact – dissolution pattern. At greater flow rates, however, instabilities begin to develop, which can evolve into ramified wormholes (Daccord & Lenormand 1987; Fredd & Fogler 1998*b*; Golfier *et al.* 2002).

Classical models of dissolution in porous media use representative elementary volume (REV)-based equations to describe the dynamics (Shapiro & Brenner 1988; Mauri 1991; Edwards, Shapiro & Brenner 1993; Guo, Quintard & Laouafa 2015). Important challenges associated with such approaches relate to the relationship between permeability, porosity and the macroscopic representation of the dissolution rate. On the one hand, changes in the pore space depend on the details of the competition between the transport and the reactions, which ultimately determines the evolution of the porosity, permeability and specific surface area of the rock. On the other hand, it is difficult to come up with a universal formulation for the dissolution rate at the REV scale (i.e. aggregate of solid and fluids) even for a mono-mineral rock. Indeed, it is known that using a simple volume averaged dissolution rate to upscale the local mass surface flux from pore to core and larger scales leads to an overestimation of the reaction rate by several orders of magnitude (Swoboda-Colberg & Drever 1993; Li, Peters & Celia 2006). These difficulties come from the fact that an REV-based dissolution rate described by averaged concentrations and the geometric specific area is not appropriate because the solid surface accessible to the acid depends strongly on the local flow conditions.

As illustrated in figure 1, the velocity distribution in the pore space of a sandstone replica (see Roman *et al.* (2016) for further details) reflects the presence of preferential flow regions and some low-velocity zones. In such configurations, the species transport may be dominated by convection in the fast regions and by diffusion in the slow zones. Hence, for high Péclet numbers, the acid ions cannot reach the surface mineral in the slow zones. The correction factor that reduces the geometric specific area to the reactive surface available to the chemical components is a critical parameter for macroscopic (REV) dissolution models. It is sometimes lumped altogether with the local constant of reaction to form the so-called effective reaction rate (Shapiro & Brenner 1988; Mauri 1991; Edwards *et al.* 1993; Panga, Ziauddin & Balakotaiah 2005; Kalia & Balakotaiah 2007; Cohen *et al.* 2008; Varloteaux, Békri & Adler 2013*a*; Guo *et al.* 2015). The accessible surface area is a very difficult quantity to obtain *a priori* because it is a complex function of the local flow condition and the solid geometry. The difficulties associated with the prediction of large-scale dissolution properties increase for natural rocks because they usually consist of multiple minerals, such as calcite, clay, quartz, dolomite and pyrite. These different minerals have very different reaction rates, and that adds to the challenge of REV-scale dissolution models (Noiriel, Madé & Gouze 2007; Landrot *et al.* 2012).

https://doi.org/10.1017/jfm.2017.499 Published online by Cambridge University Press

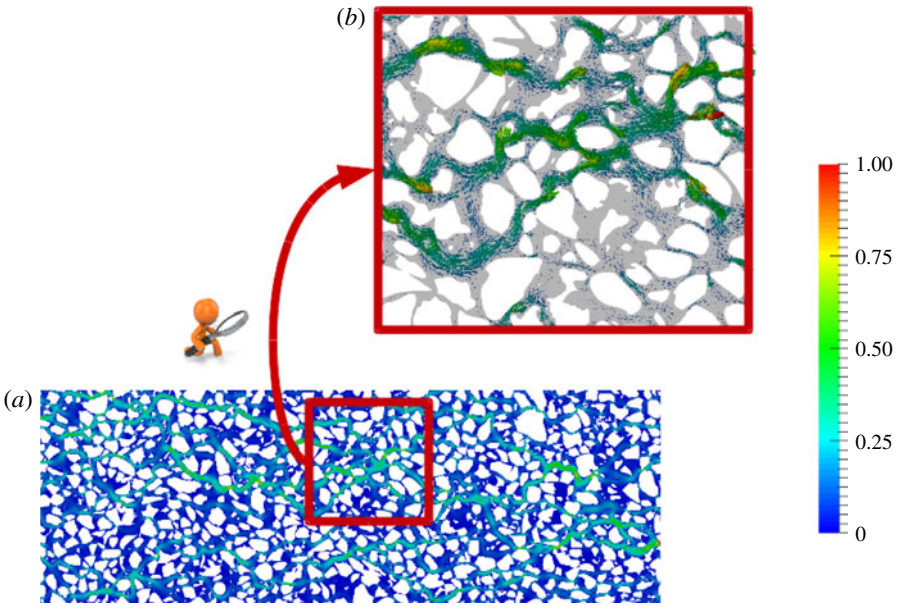


FIGURE 1. (Colour online) Plot of Stokes simulation results in a sandstone replica two-dimensional pore network. The velocity fields are normalized by the largest value. (*a*) Magnitude of the velocity field, (*b*) velocity vectors in a zoom in.

In this paper, we study the dissolution of mono-mineral rocks at the pore scale where the solid skeleton is fully described.

Different techniques have been proposed to estimate the reactive mass transfer at the pore scale. The pioneering work of Békri, Thovert & Adler (1995) entailed solving the Stokes equations combined with a 'cell-based' dissolution rate. Techniques using the arbitrary-Lagrangian–Eulerian (ALE) framework solve the full physics at the pore scale on an Eulerian grid (i.e. the Navier–Stokes equations, the transport equation and the chemical reaction at the solid boundaries) and then update the grid in time (Luo *et al.* 2012; Oltéan, Golfier & Buès 2013; Starchenko, Marra & Ladd 2016; Soulaine & Tchelepi 2016*b*). ALE techniques are very accurate in the sense that no assumptions are made about the solid geometry, and that the governing equations of continuum mechanics are solved with high accuracy. They are, however, limited to a few grains due to the re-meshing process; thus, the ALE approach cannot be used to simulate the evolution of the pore space for systems that involve large numbers of grains. Moreover, they cannot handle phenomena such as grain disappearance without sophisticated re-meshing strategies. ALE methods can serve, however, as reference solutions for validating other numerical approaches. Alternative methods use the level set function to transport the fluid–solid interface with immersed reactive boundaries on an Eulerian grid during the dissolution processes (Li, Huang & Meakin 2010; Huang & Li 2011; Xu *et al.* 2012; Varloteaux *et al.* 2013*b*; Trebotich & Graves 2015). Other works rely on the lattice Boltzmann method (LBM) for reactive mass transfer in porous media (Kang, Zhang & Chen 2003; Szymczak & Ladd 2004, 2009; Chen *et al.* 2014; Huber, Shafei & Parmigiani 2014; Kang *et al.* 2014) or pore network models (PNM) (Algive, Bekri & Vizika 2010; Kim, Peters & Lindquist 2011; Varloteaux *et al.* 2013*a*,*b*). For LBM-based approaches, collision operators at the solid walls have to be

https://doi.org/10.1017/jfm.2017.499 Published online by Cambridge University Press

determined to describe the surface chemical reactions. In PNM methods, the pore-scale physics is not solved directly. Instead, the void of a rock is first approximated as a network of throats and pore bodies. Then, the governing laws are obtained from the integration of the Navier–Stokes and transport equations in regard to the throat radius including chemical reactions at the solid surface. At every time step, the pore throat diameters are updated to balance the total mass of the system. Other methods based on the Darcy–Brinkman–Stokes (DBS) equation (Brinkman 1947) for numerical modelling of dissolution processes in porous media have also been proposed (Liu & Ortoleva 1996; Liu *et al.* 1997; Ormond & Ortoleva 2000; Golfier *et al.* 2002; Luo *et al.* 2012, 2014, 2015; Guo, Laouafa & Quintard 2016*a*; Soulaine & Tchelepi 2016*a*).

DBS approaches are Eulerian methods that employ a single equation to simulate Stokes flow in the void regions and Darcy's law for transport through the matrix. They are referred to as a micro-continuum DBS approach (Soulaine *et al.* 2016; Soulaine & Tchelepi 2016*a*) in the sense that the governing laws arise from the integration of Navier–Stokes-based equations over a control volume that may contain a solid phase, and that they are applied to small domains. With these volume averaged equations, the solid matrix is differentiated from the void (fluid filled) region based on the volume fraction of solid per cell, or control volume. A very important feature of the micro-continuum equations is that they simplify to the classic pore-scale physics in the absence of solid in the control volume.

DBS approaches were first proposed to simulate flow in a fracture surrounded by a porous medium where the volumes of fracture are discretized fully using control volumes, and the flow in them is described by the Navier–Stokes equations (Neale & Nader 1974). Micro-continuum models for heterogeneous reactive mass transfer have been proposed by Golfier *et al.* (2002) and successfully applied to the simulation of ramified wormholes induced by the injection of acid in carbonate cores. Their approach, where a porous media formulation with a non-equilibrium model is used for transport of the acid species in addition to chemical reactions with the solid minerals, is valid at the core scale. The challenges, however, to model permeability–porosity relationships and the dissolution rate in the matrix are those associated with the porous media formalism: how to estimate the effective surface area; how does the dissolution rate depend on the flow conditions; how the mass transfer coefficient(s) depend on the Péclet and Damköhler numbers?

In this paper, we propose a micro-continuum model for flow with chemical reactions at the solid surface that works at the pore scale, i.e. the solid grains (matrix) are treated as an impermeable porous medium and boundary conditions at the solid surface arise automatically from the formulation of the governing laws as immersed boundaries. A recent investigation has already demonstrated that DBS approaches can reproduce no-slip boundary conditions at the solid walls if the permeability of the porous region is small enough (Soulaine & Tchelepi 2016*a*). In this work, we develop a micro-continuum model with immersed boundary conditions for reactive mass transfer at the solid surface. This model is then used as a basis to upscale the flow properties, including the dissolution rate and the porosity/permeability relationship.

This paper is organized as follows. Next, we introduce the mathematical and numerical models of the micro-continuum approach for dissolution at the pore scale. Then, for numerical validation, we compare the micro-continuum approach with reference ALE-based solutions for single grain dissolution and we compare simulation results with the dissolution of a crystal of calcite in a micro-model

https://doi.org/10.1017/jfm.2017.499 Published online by Cambridge University Press

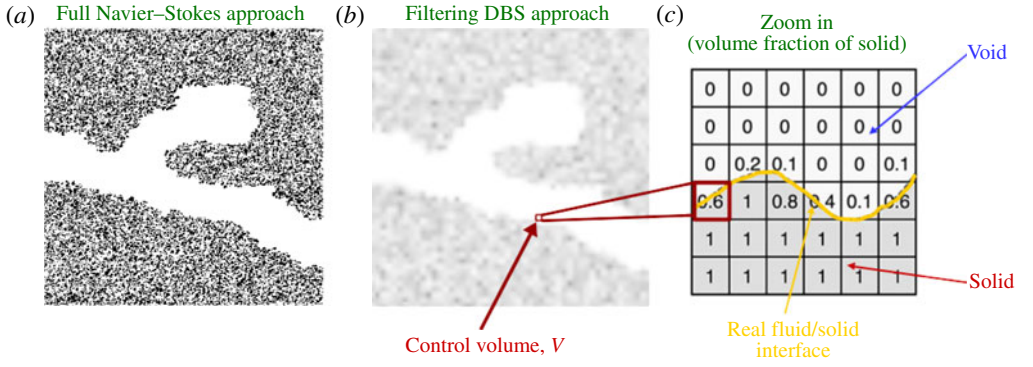


FIGURE 2. (Colour online) Representation of the void and solid with a full Navier–Stokes approach and a filtering approach. (*a*) In the former, all the solid grains are explicitly described, the flow is governed by Navier–Stokes everywhere in the void and a no-slip boundary is specified at the grain boundary. (*b*) In the latter, a cutoff length is introduced by means of the control volume V and the void is represented by the volume fraction, ε_f. (*c*) If $\varepsilon_f = 1$ (or $\varepsilon_s = 0$), here in the large channel, the flow is governed by Navier–Stokes equations. Intermediate values, $0 < \varepsilon_f < 1$ (or $0 < \varepsilon_s < 1$), correspond to the fluid/solid interface. For $\varepsilon_f = 0$ (or $\varepsilon_s = 1$), the control volumes contain solid only and there is no flow.

experiment. Following that, we use the DBS formulation to simulate dissolution in more complex pore structures and to upscale the results to a Darcy scale. We finally discuss the emergence of wormholes according to the flow conditions. We close with a summary and conclusions.

2. Mathematical model

In this section, we introduce the mathematical model used to simulate dissolution processes in porous media at the pore scale. Then, we describe the methodology to upscale flow properties to the scale of an REV.

2.1. *Pore-scale model*

Instead of a full Navier–Stokes approach as is common for pore-scale simulations (see figure 2*a*), the model adopts a micro-continuum formulation, whereby an arbitrary cutoff length is introduced and all the information regarding the solid structure below this length scale are filtered and modelled as a porous medium. Mathematically, this cutoff length is associated with a control volume, V, that corresponds to a cell of the computational grid, and all the variables of the system are averaged over V. The control volumes that contain void only, also called clear fluid regions or free zones, and those that contain solid are differentiated by ε_f, which is the volume fraction of void space within a control volume. It is defined as a field with different values all over the domain that range from 0 to 1. This filtering is illustrated in figure 2(*b*,*c*). The free zone is characterized by $\varepsilon_f = 1$, whereby the flow is governed by Navier–Stokes equations in these areas. For intermediate values, $0 < \varepsilon_f < 1$, there are solid obstacles in the control volume, and the flow is governed by Darcy's law. When $\varepsilon_f = 0$, the control volume contains solid only, and there is no flow. Actually, to make the governing equations described below valid all over the computational domain, i.e. in

https://doi.org/10.1017/jfm.2017.499 Published online by Cambridge University Press

the free and the solid regions, we assume that the cells describing solid regions always contain a tiny porosity, $\varepsilon_f = 0 \equiv 0.001$. Different from other micro-continuum models proposed to simulate core-scale phenomena (Liu *et al.* 1997; Ormond & Ortoleva 2000; Golfier *et al.* 2002; Scheibe *et al.* 2015; Soulaine & Tchelepi 2016*a*), here we use a DBS formulation to simulate the pore-scale physics. So, only the bounding values $\varepsilon_f = 1$ and $\varepsilon_f = 0$ are used to describe the porous structure at the pore scale. The intermediate values of void (or volume of solid) describe the interface between fluid and solid (see figure 2*c*). The interface is not necessarily sharp and can be spread over several cells. So, this model belongs to the family of the diffuse interface models. Note that by definition, the relation

$$\varepsilon_s + \varepsilon_f = 1, \tag{2.1}$$

where ε_s is the volume fraction of solid, and ε_f the volume fraction of void, is always valid.

Likewise, the other variables of the system are defined as averaged quantities over the control volume (Whitaker 1999). The pressure and acid mass fraction are intrinsic phase averages, $\bar{p}_f = (1/V_f)\int_{V_f} p_f \,\mathrm{d}V$ and $\bar{\omega}_{f,A} = (1/V_f)\int_{V_f} \omega_{f,A}\,\mathrm{d}V$ respectively, where V_f is the volume occupied by the fluid in the control volume and the velocity is defined as a superficial average, $\bar{\boldsymbol{v}}_f = (1/V)\int_{V_f} \boldsymbol{v}_f \,\mathrm{d}V$, in agreement with Darcy's law.

The flow model arises from the integration of the Navier–Stokes momentum equation over a control volume in the presence of solid material (Vafai & Tien 1981, 1982; Hsu & Cheng 1990; Bousquet-Melou *et al.* 2002). The averaging process results in a single equation that holds in both the free flow and the porous medium domains. We have,

$$\frac{1}{\varepsilon_f}\left(\frac{\partial \rho_f \bar{\boldsymbol{v}}_f}{\partial t} + \boldsymbol{\nabla}\cdot\left(\frac{\rho_f}{\varepsilon_f}\bar{\boldsymbol{v}}_f\bar{\boldsymbol{v}}_f\right)\right) = -\boldsymbol{\nabla}\bar{p}_f + \frac{\mu_f}{\varepsilon_f}\nabla^2\bar{\boldsymbol{v}}_f - \mu_f k^{-1}\bar{\boldsymbol{v}}_f, \tag{2.2}$$

where the locally averaged pressure, $\bar{p}_f$, and velocity field, $\bar{\boldsymbol{v}}_f$, are the unknowns of the system. This equation is an extension of the original Darcy–Brinkman–Stokes equation (Brinkman 1947) with inertia in the free zone and fluid/solid mass transfer described by the terms on the left-hand side. The two first terms on the right-hand side are the pressure gradient and the diffusive viscous contribution. The last term of the right-hand side of (2.2) represents the momentum exchange term between the fluid and the solid phase, i.e. the Darcy resistance term. It vanishes in the free zone, so that (2.2) degenerates to the Navier–Stokes equations. This drag term is dominant in the solid region so that the velocity is reduced to almost zero in this region. For low values of k, i.e. at least four orders of magnitude below the permeability of the porous structure described by ε_f, it forces a no-slip boundary condition at the fluid/solid interface (Angot, Bruneau & Fabrie 1999; Khadra *et al.* 2000; Soulaine & Tchelepi 2016*a*).

During the dissolution process, the solid morphology evolves with chemical reactions at the mineral surfaces. To simplify the system, we consider one mineral only. Hence, the solid volume fraction in a control volume, ε_s, is an unknown of the system, and its evolution is governed by the mass balance equation

$$\frac{\partial \varepsilon_s \rho_s}{\partial t} = -\dot{m}, \tag{2.3}$$

where ρ_s is the solid density and $\dot{m}$ is the rate of fluid/solid mass transfer. The latter has a non-zero value only at the fluid/solid interface. All the dissolved mass goes into

https://doi.org/10.1017/jfm.2017.499 Published online by Cambridge University Press

the fluid phase, and the continuity equation for the fluid phase reads

$$\frac{\partial \varepsilon_f \rho_f}{\partial t} + \boldsymbol{\nabla} \cdot \left(\rho_f \bar{\boldsymbol{v}}_f\right) = \dot{m}, \tag{2.4}$$

where ρ_f is the fluid density. In this study, ρ_f is considered constant and independent of the fluid composition.

The solid is dissolved by an acid denoted A. Because A is the only species in the fluid phase that reacts with the solid phase, it is the only concentration in the fluid mixture solved in this model. The mass balance equation averaged over the control volume is

$$\frac{\partial \varepsilon_f \rho_f \bar{\omega}_{f,A}}{\partial t} + \boldsymbol{\nabla} \cdot \left(\rho_f \bar{\boldsymbol{v}}_f \bar{\omega}_{f,A}\right) = \boldsymbol{\nabla} \cdot \left(\varepsilon_f \rho_f D_A^* \boldsymbol{\nabla} \bar{\omega}_{f,A}\right) - \dot{m}_A, \tag{2.5}$$

where D_A^* denotes the effective diffusivity of species A into the fluid mixture, and $\dot{m}_A$ is the rate of the chemical reaction of A with the solid minerals. As for $\dot{m}$, this term is non-zero only in the presence of solid minerals. To account for tortuosity in the cell matrix, the effective diffusivity is $\varepsilon_f D_A^* = \varepsilon_f^2 D_A$, where D_A is the molecular diffusivity of the acid into the fluid mixture (Wakao & Smith 1962). Note that in the free zone, $\varepsilon_f = 1$, and (2.5) degenerates to the classic advection–diffusion equation.

The mathematical problem formed by (2.2)–(2.5) is valid over the entire Eulerian grid whether the cell contains solid, or void. Importantly, in the clear fluid region, all the equations degenerate to the standard conservation laws of fluid mechanics. In the solid regions, the drag force term drops the velocity value to near zero, which enforces a no-slip boundary condition at the fluid/solid interface. During the dissolution process, the interface moves, and the local permeability field, k, has to be updated according to the solid distribution in the computational grid. A Kozeny–Carman relation

$$k^{-1} = k_0^{-1} \frac{(1-\varepsilon_f)^2}{\varepsilon_f^3}, \tag{2.6}$$

is used here to estimate the local permeability as a function of porosity. Indeed, a Kozeny–Carman permeability–porosity relationship allows (2.2) to switch asymptotically from the continuum behaviour, where Darcian friction is dominant, to the Navier–Stokes pure fluid behaviour according to the cell porosity values: in the free zones, $\varepsilon_f = 1$, and then $k^{-1} = 0$. In this equation, k_0^{-1} is an input parameter that needs to be small enough. We have found that at least four orders of magnitude below the permeability of the sample are necessary to ensure the no-slip boundary condition.

The last ingredient of the model concerns the formulation of the mass exchange terms, $\dot{m}$ and $\dot{m}_A$. First, the rate of dissolved mass is obtained from a simple mass balance

$$\dot{m} = \beta \dot{m}_A, \tag{2.7}$$

where β is a stoichiometric coefficient. To calculate, $\dot{m}_A$, we consider a first-order reaction rate, so the acid boundary condition at the solid surface is formulated as

$$\boldsymbol{n}_{fs} \cdot \left(\rho_f \left(\boldsymbol{v}_f - \boldsymbol{w}\right) \omega_{f,A} - \rho_f D_A \boldsymbol{\nabla} \omega_{f,A}\right) = r \rho_f \omega_{f,A}, \tag{2.8}$$

where $\boldsymbol{n}_{fs}$ is the normal at the fluid/solid interface, $\boldsymbol{w}$ is the receding velocity of this interface due to the surface chemical reaction and r is the reaction rate constant. A mass balance gives $\boldsymbol{n}_{fs} \cdot \boldsymbol{w} = -r(\rho_f/\rho_s)\beta \omega_{f,A}$. The model presented in this paper has a

https://doi.org/10.1017/jfm.2017.499 Published online by Cambridge University Press

micro-continuum formulation, which means that the flux boundary condition, equation (2.8), is not imposed directly at the edge of the computational grid, but instead is imposed as an immersed boundary condition. This is achieved by integrating (2.8) over a control volume; hence, the flux can be formulated as

$$\begin{aligned}\dot{m}_A &= \frac{1}{V}\int_{A_{fs}} \boldsymbol{n}_{fs}\cdot\left(\rho_f\left(\boldsymbol{v}_f-\boldsymbol{w}\right)\omega_{f,A}-\rho_f D_A\nabla\omega_{f,A}\right)\,\mathrm{d}A,\\ &= \frac{1}{V}\int_{A_{fs}} r\rho_f\omega_{f,A}\,\mathrm{d}A,\\ &\approx a_v r\rho_f\bar{\omega}_{f,A},\end{aligned} \tag{2.9}$$

where a_v is the effective surface area in one cell of the Eulerian grid. To obtain (2.9), the spatial variations of the concentration inside a control volume are neglected and $\omega_{f,A}\approx\bar{\omega}_{f,A}$. This assumption corresponds to the discretization error. Because we use a micro-continuum formulation for pore-scale simulation, there is a sharp transition between the clear fluid region and the solid region (see figure 2*c*). Hence, the surface area per control volume is $a_v=\|\nabla\varepsilon_f\|$. This relationship between the specific area and the porosity gradient arises from the volume averaging theorem, $-\nabla\varepsilon_f=(1/V)\int_{A_{fs}}\boldsymbol{n}_{fs}\,\mathrm{d}A$, that relates the gradient of porosity to the average surface normal in a control volume (Whitaker 1999). To enforce the localization of the reactive boundary solution at the fluid/solid interface, the specific area is computed as $a_v=\|\nabla\varepsilon_f\|\psi$, where ψ is a function that characterizes the diffuse interface. Several functions have been proposed by Luo *et al.* (2012) to compute ψ. In this work, we use $\psi=4\varepsilon_f(1-\varepsilon_f)$. Hence, a_v is non-zero only at the immersed solid/fluid interface, and therefore $\dot{m}_A$ is a body source term even though it is applied only at the solid boundaries.

The mathematical problem introduced in this section has been implemented in the open-source simulation platform OpenFOAM® (http://www.openfoam.org). Equations (2.2)–(2.5) are first discretized with the finite-volume method and solved sequentially. The pressure–velocity coupling is handled by a predictor–corrector strategy based on the pressure implicit with splitting of operators algorithm (Issa 1985). All the information regarding the numerics is found in Soulaine & Tchelepi (2016*a*).

2.2. *Upscaling to the Darcy scale*

Simulation results at the pore scale with the micro-continuum approach are used to characterize flow properties at the REV scale. This is achieved by averaging the results over the large-scale control volume, $\mathcal{V}$, with the volume average operators $\langle\cdot\rangle=(1/\mathcal{V})\int_{\mathcal{V}}\cdot\,\mathrm{d}V$ and $\langle\cdot\rangle^f=(1/\mathcal{V}_f)\int_{\mathcal{V}_f}\cdot\,\mathrm{d}V$ where $\mathcal{V}_f$ is the volume of fluid in the control volume $\mathcal{V}$. The porosity of the porous medium, ϕ, is obtained by averaging the local void fraction field in the REV,

$$\phi=\langle\varepsilon_f\rangle. \tag{2.10}$$

The geometric specific surface of the porous medium, A_e, is computed by volume averaging the local effective surface area,

$$A_e=\langle a_v\rangle=\langle\|\nabla\varepsilon_f\|\rangle. \tag{2.11}$$

https://doi.org/10.1017/jfm.2017.499 Published online by Cambridge University Press

The permeability of the REV, K, is obtained by computing the averaged velocity and the pressure gradient in $\mathcal{V}$ and using Darcy's law,

$$\langle \bar{\boldsymbol{v}}_f \rangle = -\frac{K}{\mu_f} \boldsymbol{\nabla} \langle \bar{p}_f \rangle^f. \tag{2.12}$$

To upscale the dissolution rate, we consider the REV-scale formulation, namely,

$$\langle \dot{m}_A \rangle = A_e \alpha r \rho_f \langle \bar{\omega}_{f,A} \rangle^f, \tag{2.13}$$

where α is a correction factor that varies between 0 and 1. It accounts for the actual area available to the chemical components compared with the nominal area. Combining (2.9) and (2.13), the correction factor is computed as follows:

$$\alpha = \frac{\langle a_v \bar{\omega}_{f,A} \rangle}{A_e \langle \bar{\omega}_{f,A} \rangle^f}. \tag{2.14}$$

The effective parameters, K and α, depend strongly on the flow conditions. To characterize them, we define a set of dimensionless numbers. The flow is characterize by the Reynolds number, which quantifies inertia effects compared with the viscous forces

$$Re = \frac{\rho_f v_0 l}{\mu_f} = \frac{\rho_f v_0 \sqrt{K}}{\mu_f}, \tag{2.15}$$

where v_0 is a characteristic velocity (usually the inlet velocity) and l is a characteristic length. For flow problems, l is related to the pore throat diameters in a flow pathway and scales as the square root of the permeability of the porous medium. All the simulations reported here exclude inertial effects, so we always have $Re < 1$. Similarly, the transport processes of the acid species in the pore space are characterized by the Péclet number defined as the ratio of the advection rate of a chemical species by the flow to the rate of diffusion of this quantity in the fluid mixture, that is,

$$P\acute{e} = \frac{v_0 l}{D_A} = \frac{v_0 \sqrt{K}}{D_A}. \tag{2.16}$$

As for the chemical reaction at the solid surface described by the boundary condition (2.8), it is characterized by the so-called second Damköhler number defined as the ratio of the reaction rate and the diffusive mass transfer rate at the fluid/solid interface,

$$Da_{II} = \frac{r l'}{D_A} = \frac{r}{A_e D_A}. \tag{2.17}$$

Because the reaction occurs at the solid surface, the characteristic length, l', involved in this process is the specific area of the medium. Note that Da_{II} varies with both the molecular diffusivity and the reaction rate constant. The ratio of the Damköhler and Péclet numbers is also a relevant quantity in characterizing the flow conditions, namely,

$$Da_I = \left(\frac{Da_{II}}{P\acute{e}} \right) = \frac{r}{v_0 \sqrt{K} A_e}. \tag{2.18}$$

https://doi.org/10.1017/jfm.2017.499 Published online by Cambridge University Press

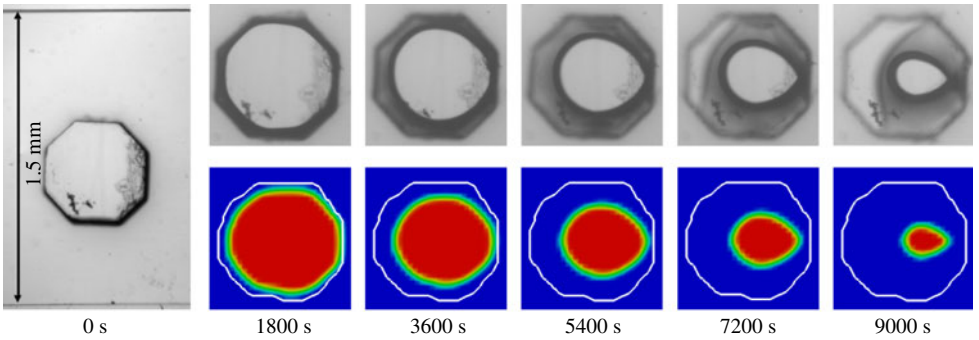


FIGURE 3. (Colour online) Experimental (top) and simulation (bottom) images of calcite dissolution process at different time steps. The acid concentration is 0.05 % HCl injected at a mean velocity of 1.16×10^{-3} m s^{-1}.

3. Validation of the methodology

In this section, we illustrate the potential of a DBS based approach for modelling dissolution of solid minerals at the pore scale. First, we compare the simulation results with experimental observations of the dissolution of a calcite crystal in a micro-model. Then, we focus on the dissolution of a single grain and compare the results with simulations based on an arbitrary Lagrangian–Eulerian framework.

3.1. *Comparison with micro-model experiments*

For verification, the DBS prediction are compared with experimental data. The experimental set-up consists of a straight polydimethylsiloxane (PDMS) micro-channel with a 1.5 mm $\times$ 0.2 mm cross-section. A calcite post, an octagonal prism with a width of 0.5 mm and a height of 0.25 mm, is placed at the centre of the micro-channel. A syringe pump (Harvard Apparatus Pump 11 Elite, accuracy 0.5 %) connected to a plastic syringe (BD, 10 ml) containing the acid solution provides a constant injection rate of 3.5×10^{-10} m^3 s^{-1} into the micro-channel. This corresponds to a mean velocity of 1.16×10^{-3} m s^{-1}, representative of the near-well injection rate. The injected fluid is a mixture of deionized water, 50 % ethanol (EtOH), and 0.05 % hydrogen chloride (HCl). The PDMS channel walls are hydrophobic; thus, ethanol is added to the acid mixture in order to wet the PDMS. The micro-channel is placed under a Nikon ME600 microscope. Direct visualization of the dissolution dynamics is recorded using a pco.edge 5.5 camera (sCMOS sensor up to 50 f.p.s.).

Sequences of images of the dissolution process are recorded and analysed in order to measure the evolution of the size of the calcite post. Figure 3, shows images of the calcite post at different times during the dissolution process. In these images, we observe the initial calcite edges, even when it is completely dissolved. This is because the calcite post is stuck in the PDMS initially. The calcite is completely dissolved after 11 200 s (about 3 h). The shape of the calcite as it dissolves is influenced by the hydrodynamics in the void space: it deviates from the hexagonal shape to a petal-like shape with the tip downstream, where the local dissolution rate is lower because this area is a stagnant zone.

The evolution of the total mass of the solid and the interfacial area are measured from the top view of the micro-channel assuming a homogeneous dissolution in the channel depth. According to this two-dimensional-process assumption, the area of

https://doi.org/10.1017/jfm.2017.499 Published online by Cambridge University Press

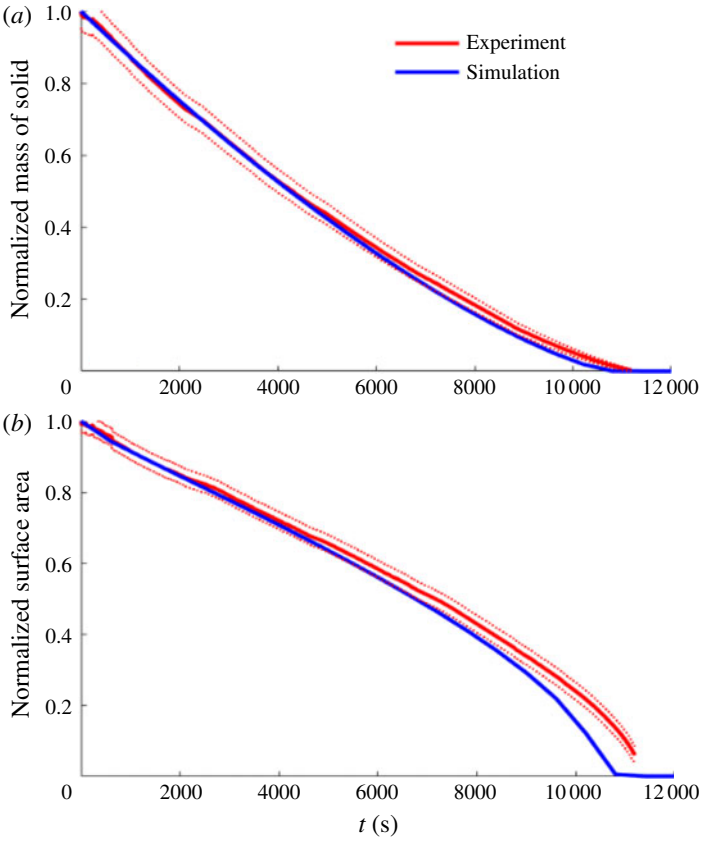


FIGURE 4. (Colour online) (*a*) Plot of the evolution of the total mass of solid in the micro-channel normalized by the mass at $t=0$ s. (*b*) Plot of the evolution of the interfacial area normalized by the calcite area at $t = 0$ s. The dashed lines correspond to the experimental uncertainties.

the calcite measured by image processing, plotted in figure 4(*a*), is equivalent to the evolution of the total mass of the solid. The measurement of the contour of the calcite in the images, plotted in figure 4(*b*), gives the evolution of the interfacial area. Both curves are normalized by the initial values. By considering 10 pixels of uncertainty on the detection of the calcite contour by image processing, we have an error of approximately 5 % for the total mass of the solid and approximately 2.8 % for the interfacial surface area. The experimental uncertainties are represented by the red-dashed lines.

The DBS simulation framework is compared with the experimental data. The computational domain is a three-dimensional (3-D) 2.6 mm $\times$ 1.5 mm $\times$ 0.2 mm box discretized with a $125 \times 75 \times 5$ Cartesian grid (47×10^3 cells). All the walls of the box are impermeable with no chemical reaction. The image of the calcite crystal in the micro-channel before the injection of acid is used to initialize the cell porosity. Specifically, we set to $\varepsilon_f = 0.001$ for the cells containing the crystal and $\varepsilon_f = 1$ elsewhere. A solution of 0.05 % of acid is injected from the left-hand side of the domain at a constant velocity $v_0 = 1.16 \times 10^{-3}$ m s^{-1}. For the ethanol/water mixture, the viscosity and density are $\mu_f = 2.4 \times 10^{-3}$ Pa s and $\rho_f = 920$ kg m^{-3}.

https://doi.org/10.1017/jfm.2017.499 Published online by Cambridge University Press

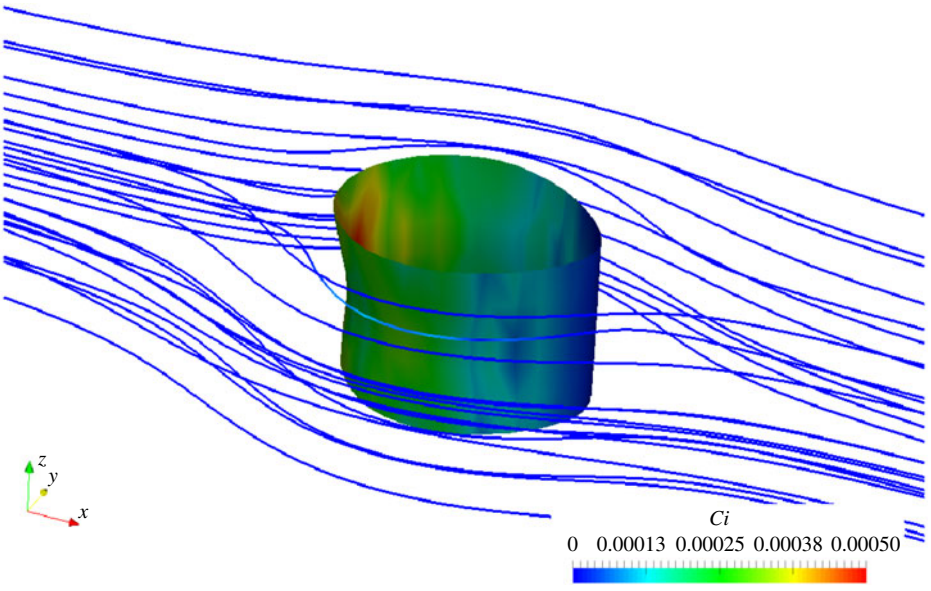


FIGURE 5. (Colour online) Contour of the calcite crystal coloured based on the concentration profile 120 min after acid injection. The blue lines correspond to the streamlines.

The diffusion of HCl in the mixture is $D_A = 5 \times 10^{-9}$ m^2 s^{-1}, the calcite density is $\rho_s = 2710$ kg m^{-3}, and the stoichiometric coefficient is $\beta = (M_{CaCO_3}/2M_{HCl}) \approx 1.37$. The constant of reaction is $r = 5 \times 10^{-3}$ m s^{-1}. We obtained this value based on a trial-and-error approach until the best fit with experimental data was obtained. These parameters correspond to $Pé \approx 15$ and $Da_{II} \approx 5 \times 10^2$. The simulation is run for 12 000 s and the results are output every 10 min.

Simulation results for the evolution of the calcite crystal in the mid-plane at different times are plotted in figure 3. The results are in very good agreement with the micro-model experiment. In particular, the elongated shape of the crystal during the dissolution process is well captured by the numerical model. As illustrated in figure 5 that represents the calcite crystal coloured by concentration profile 120 min after acid injection, there are no major 3-D effects in the crystal thickness. Eventually, the upstream calcite profile, where the acid concentration is more important, is slightly concave following the parabolic flow profile in Hele-Shaw cells. The downstream contour of the calcite crystal is almost flat. This justifies *a posteriori* the 2-D assumption used to post-treat the evolution of the mass of solid and of the interfacial area from the sequences of images. These two data obtained numerically are plotted in figure 4. The results are very good and the experimental and numerical curves are almost on top of each other. Many reasons explain the slight discrepancies. First, the DBS approach approximates the solid shape by a stairwise geometry. Second, uncertainties come from the formulation of the local reaction rate as a first-order reaction and the estimation of constant of reaction. Indeed, the roughness of the crystal surface may impact the value of the constant of reaction when it is replaced by an effective surface (Guo, Veran-Tissoires & Quintard 2016*b*) as in the DBS approach. Nevertheless, the results are still very good, and the DBS framework for pore-scale dissolution can be used with confidence to investigate the upscaling of dissolution phenomena in porous media.

https://doi.org/10.1017/jfm.2017.499 Published online by Cambridge University Press

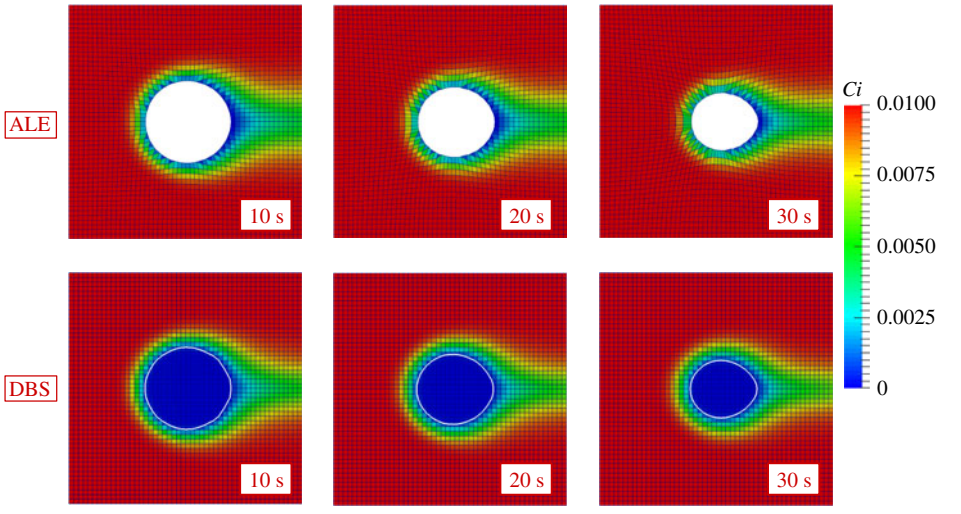


FIGURE 6. (Colour online) Simulation results for the dissolution of a single pillar with ALE and DBS approaches. Both methods are in very good agreement.

3.2. *Comparison with ALE simulations*

We compare the DBS model with simulations performed with an ALE framework. ALE is considered as a reference solution for the pore-scale dissolution problem. We validate the immersed boundary formulation introduced with the micro-continuum model for reactive mass transfer at the surface of minerals against ALE simulation. The geometry is a 200 μm $\times$ 200 μm two-dimensional box that contains a cylindrical pillar in the middle. We consider two grids for the DBS simulations: 50 $\times$ 50 and 75 $\times$ 75 Cartesian grids. The cell porosity is set to $\varepsilon_f = 0.001$ for the cells that make up a cylinder of 76 μm in diameter centred in the middle of the domain. Everywhere else, $\varepsilon_f = 1$. Hence, the edge of the pillar is approximated as a stairwise surface. The top and bottom boundaries are set as impermeable fixed walls with no reaction. A solution of one per cent of acid by weight is injected from the left-hand side of the domain at a constant velocity, $v_0 = 10^{-3}$ m s^{-1} for 30 s. The right-hand side is an outflow condition. The other properties are $\mu_f = 10^{-3}$ Pa s, $\rho_f = 1000$ kg m^{-3}, $\rho_s = 2165$ kg m^{-3}, $\beta = 1$, $D_A = 10^{-9}$ m^2 s^{-1}, $r = 10^{-2}$ m s^{-1} and $k_0 = 10^{-15}$ m^2.

With the ALE formulation, only the void space is gridded. Hence, starting from a 50 $\times$ 50 Cartesian grid, the cells that contain the solid pillar are removed, and tetrahedral cells are introduced to represent the cylindrical geometry. The incompressible Navier–Stokes equations and a standard advection/diffusion equation are solved with OpenFOAM® to transport the acid concentration in the computational domain. The ALE approach requires boundary conditions at the solid surface, namely a no-slip boundary condition and the reactive condition, equation (2.8). Moreover, the surface reaction leads to dissolution of the solid, which means that the geometry of the solid evolves during the process. A mass balance provides the value of the receding velocity, $\boldsymbol{w}$, at every point of the solid surface, $\boldsymbol{n}_{fs} \cdot \boldsymbol{w} = -r(\rho_f/\rho_s)\beta\omega_{f,A}$. The points of the grid at the reactive surface are moved accordingly, and a Laplace equation is solved for the motion of all the points of the grid in order to have homogeneous deformations.

The simulation results obtained using the two approaches are plotted in figure 6 which shows very good agreement. For both approaches, the pillar deviates from its

https://doi.org/10.1017/jfm.2017.499 Published online by Cambridge University Press

cylindrical shape during the dissolution process. This is the result of the complex interplay between transport and surface reaction. Indeed, the right side of the pillar creates a stagnant zone for the flow where the acid concentration is smaller. Hence, the local dissolution rate in the downstream area of the pillar is less than in the region facing the domain inlet, and that leads to the shape asymmetry. Further details regarding the calcite shape during the dissolution process are discussed in § 4.1. After 30 seconds of dissolution, the difference of the mass of solid between the ALE and DBS simulations is less than 5 %. Moreover, for both cases, we checked with refined grids (75 cell $\times$ 75 cell) that the simulations reach mesh convergence.

These results validate the DBS approach applied to the simulation of dissolution phenomena at the pore scale. In particular, they demonstrate that the mass flux formulated as a body force recovers the physical boundary conditions at the solid surface.

4. Upscaling dissolution processes and wormholing

In this section, we use the DBS framework to upscale the dissolution rate under various flow conditions. Then, we investigate the dissolution pattern in a more complex pore space and we discuss the conditions that lead to different of wormhole regimes.

4.1. *Pore-scale simulation of model porous media*

We use the DBS framework to investigate the effective properties of a model porous medium. Specifically, we investigate the permeability–porosity relationship and the macroscale representation of the dissolution rate. The geometry consists of a 2-D, 14 mm $\times$ 1 mm, tube with a 700 $\times$ 50 Cartesian grid. Ten cylinders of solid are homogeneously distributed along the tube (see figure 7). Each cylinder is initially 0.6 mm in diameter and has a reactive boundary that evolves with the injection of acid into the system. The top and bottom boundaries are impermeable fixed walls with no reaction. One per cent of acid is injected from the left-hand side of the domain at a constant velocity, $v_0 = 1.15 \times 10^{-3}$ m s^{-1}. The right-hand side of the tube is an outflow condition. Although this geometry is a very simplified representation of a porous medium, it has all the fundamental features of a porous material, i.e. it contains several representative elementary volumes (REV) with porosity, permeability and tortuosity. Initially, the porosity, permeability and specific area of a REV are numerically estimated to $\phi_0 \approx 0.717$, $K_0 = 5.6 \times 10^{-9}$ m^2 and $A_0 = 1885$ m^{-1}, respectively. This kind of set-up is often used in homogenization studies to validate upscaling processes by comparison of the upscaled solution with reference solutions obtained by volume averaging of the results obtained using direct numerical simulation (Davarzani, Marcoux & Quintard 2010). This idealized porous medium is also commonly used to investigate complex flow and transport in porous media from the pore scale and to get more insights regarding the different mechanisms involved (Soulaine *et al.* 2015).

We use this set-up to investigate the dependence of the formulation of the macroscale dissolution rate and the permeability–porosity relationship on the flow parameters. The evaluation of other macroscale parameters, such as dispersion tensor is not investigated in this study. Several simulations for various diffusivity values ($D_A = 10^{-10}$–10^{-7} m^2 s^{-1}) and local reaction rate ($r = 10^{-5}$–10 m s^{-1}) have been performed. These correspond to a parameter space covering Péclet numbers ranging from $Pé = 10^{-2}$ to 10^3 and Damköhler numbers ranging from $Da_{II} = 10^{-3}$ to 10^6

https://doi.org/10.1017/jfm.2017.499 Published online by Cambridge University Press

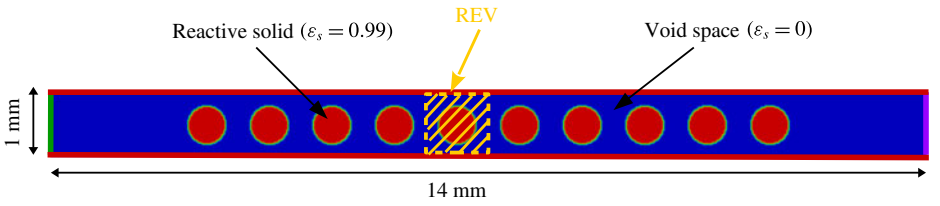


FIGURE 7. (Colour online) Geometry of the idealized porous medium used for pore-scale simulation. It is made up of a succession of REVs. Blue corresponds to the void space ($\varepsilon_f = 1$) and red to the solid ($\varepsilon_f = 0.01$). For upscaling purposes, simulation results are averaged on the fifth REV.

($(Da_{II}/Pe) = 10^{-3}$–10^{4}, respectively). The other simulation properties are set to $\mu_f = 10^{-3}$ Pa s, $\rho_f = 1000$ kg m^{-3}, $\rho_s = 2000$ kg m^{-3}, $\beta = 1$ and $k_0 = 10^{-15}$ m^2. This corresponds to the creeping flow regime ($Re \approx 0.09$).

Simulation results of the concentration of acid and of the grains boundary for different times after acid injection are plotted in figures 8–10. Concentration profiles and the solid grain geometry display very different patterns depending on the flow conditions. The second Damköhler number, Da_{II}, which characterizes the chemical reaction at the solid surface, is the appropriate dimensionless number to scale the different dissolution patterns observed.

For $Da_{II} < 1$ (see figure 8), the void space is completely saturated with the acid, and all the solid grains are surrounded by the same amount of reactant, which is consumed homogeneously at the mineral surface. Hence, throughout the dissolution process, the solid grains maintain a cylindrical shape.

For $Da_{II} > 1$, the pillars deviate from the cylindrical shape during the dissolution process, and we observe an elongation of the solid shape in the direction of the flow (see figures 9 and 10). This asymmetry of the solid shape results from heterogeneous distribution of the acid concentration at the solid surface due to the flow conditions. In turn, this leads to a heterogeneous distribution of the local dissolution rate. Indeed, in this dissolution regime, the right-hand side of the solid mineral is exposed less to the acid ions compared with the left-hand side that faces the acid injection. Moreover, at the upstream and downstream stagnation points, the flow decelerates to zero speed, and less acid ions reach the solid surface when the transport is dominated by advection causing two singularities. Hence, the local dissolution rate and, therefore, the receding velocity of the solid boundary is less important for the downstream surface than for the upstream area, which causes the pillars asymmetry. For this range of Damköhler number, we distinguish two different pillar shapes that depend on the hydrodynamics in the pore space, i.e. depend on the Péclet number. Indeed, this latter case characterizes the dispersion of the acid species in the porous medium. The two simulations presented in figures 9 and 10 share the same Damköhler number ($Da_{II} = 5 \times 10^{1}$) but differ in Péclet number ($Pé = 88$ and $Pé = 0.88$ respectively). For $Pé \geqslant 10$, the mechanisms that bring the acid ions to the mineral surface are dominated by advection. In addition to the two corners induced by the two up and downstream stagnation points already mentioned, two other angular points on the lateral faces are also observed, causing this diamond-like shape profiled in the direction of the flow. For low Péclet number ($Pé < 10$), diffusion is dominant over the convective force, and the local dissolution rate on the lateral faces is therefore more homogeneous resulting

https://doi.org/10.1017/jfm.2017.499 Published online by Cambridge University Press

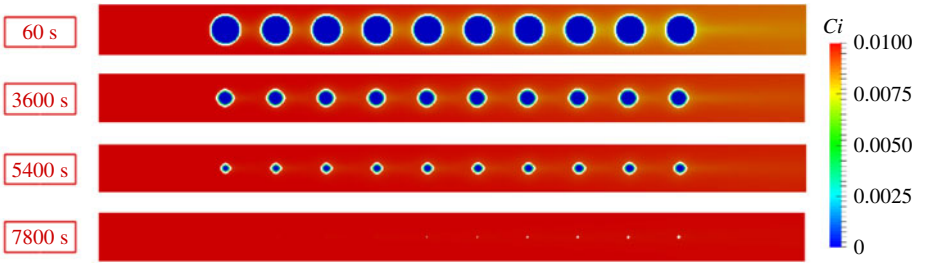


FIGURE 8. (Colour online) Plot of the acid concentration and grain boundaries for different times after acid injection for $Da_{II} = 5 \times 10^{-1}$ and $Pé = 8.8$.

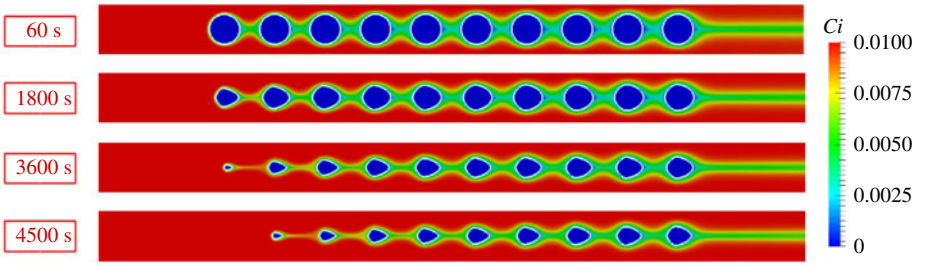


FIGURE 9. (Colour online) Plot of the acid concentration and grain boundaries for different times after acid injection for $Da_{II} = 5 \times 10^{1}$ and $Pé = 88$.

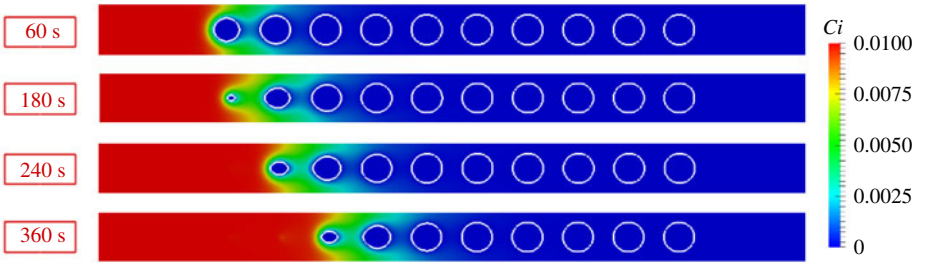


FIGURE 10. (Colour online) Plot of the acid concentration and grain boundaries for different times after acid injection for $Da_{II} = 5 \times 10^{1}$ and $Pé = 0.88$.

in a smoother shape of the dissolved pillar. Figure 11 represents a Péclet/Damköhler diagram that summarizes the different dissolution regimes identified in this section.

These three different dissolution regimes differ from one another in the reactive surface accessible by the acid species, and we have seen that this is a strong function of the Damköhler and Péclet numbers. The macroscale dissolution rate, equation (2.13), involves a correction factor, α, that represents the reduction of the reactive surface area accessible to acid contaminants due to the hydrodynamics. For all the simulation results, we computed the value of the correction factor for the first time steps for the fifth REV following the procedure described in § 2.2. The values of α are plotted in figure 12. For $Da_{II} < 1$, all the surface available reacts homogeneously with the acid. In such case, the pillars keep their cylindrical shape and $\alpha \to 1$ as theoretically demonstrated by Guo *et al.* (2015) with the method of the volume

https://doi.org/10.1017/jfm.2017.499 Published online by Cambridge University Press

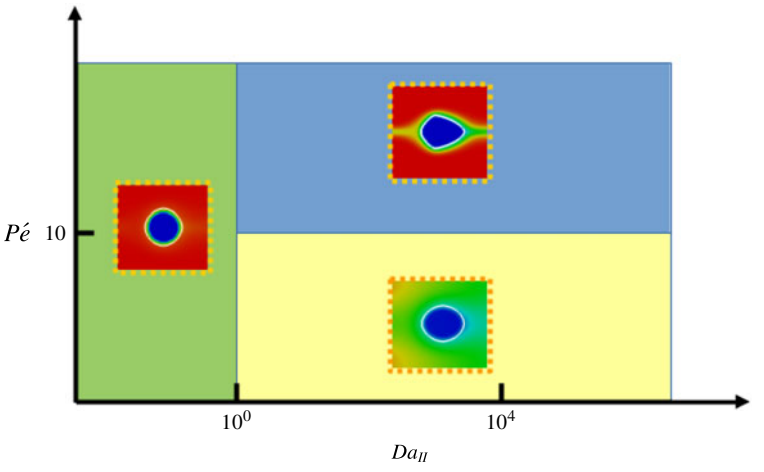


FIGURE 11. (Colour online) Regime diagram according to Péclet and Damköhler numbers.

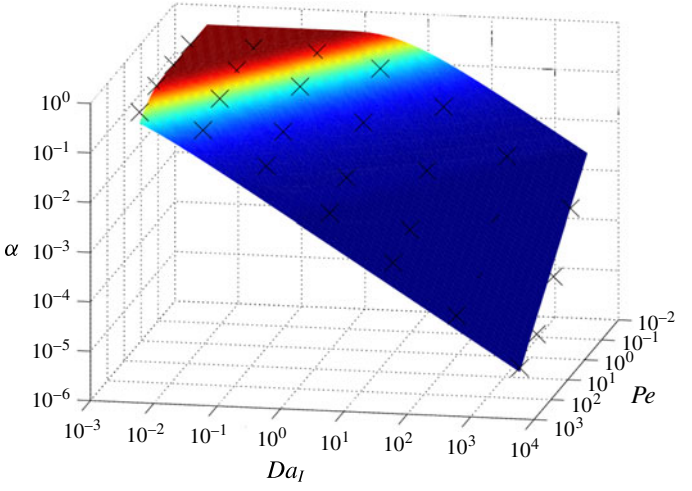


FIGURE 12. (Colour online) Plot of the correction factor, α, according to the Péclet and Damköhler numbers.

averaging. For $1 \leqslant Da_{II} < 10^4$, the correction factor decreases exponentially from 1 to 0 when Da_{II} increases (see figure 12*a*). Contrary to Guo *et al.* who suggested that the Péclet number has very low impact on the value of α, our results show a strong dependency. For larger values of the Damköhler number ($Da_{II} \geqslant 5 \times 10^4$), the correction factor tends towards zero, in agreement with the theoretical results of Mauri (1991) and Guo *et al.* (2015) who showed that $\alpha = O\left(Da_{II}^{-1}\right)$ when $Da_{II} \to \infty$. This does not mean that the average dissolution rate described by (2.13) is zero, but that it becomes independent of the constant of reaction. This situation has been observed numerically for $Da_{II} \geqslant 5 \times 10^4$ and $Pé > 10$. Nonlinear regression analysis shows that the correction factor, α, can be described by the function

$$\alpha = 1 - \exp\left(-Pé^{-n}\left(\frac{Da_{II}}{Pé}\right)^{-m}\right), \tag{4.1}$$

https://doi.org/10.1017/jfm.2017.499 Published online by Cambridge University Press

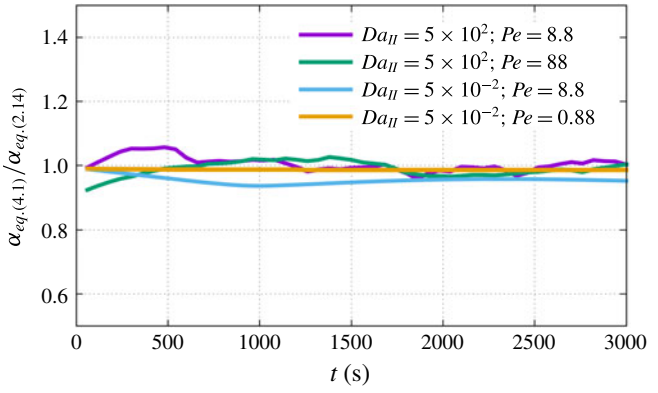


FIGURE 13. (Colour online) Plot of the evolution of the ratio between the correction factor, α, computed according to (4.1), and the correction factor computed with (2.14).

with $n = 0.53$ and $m = 0.88$ (less than 5 % of relative error). Note that $n \neq m$, which emphasizes the strong nonlinear dissolution sub-regime that depends on the Péclet number when $1 \leqslant Da_{II} < 10^4$. As the solid dissolves, the permeability, porosity and specific area evolve, and the Péclet and Damköhler numbers change accordingly. Equation (4.1) remains valid during the dissolution process as illustrated by the plot of the evolution of the ratio of α computed with (4.1), where the Péclet and Damköhler numbers are evaluated in the current state of the medium and α is computed with (2.14). Therefore, this formulation of the correction factor can be used directly to describe the dissolution rate of REV-based models.

We see from (2.13) that once the correction factor is determined, only the change of the effective surface area with time has to be estimated in order to close the system for Darcy-scale modelling. A number of different models based on geometrical constructions have been proposed to relate changes in porosity to changes in surface area (Lichtner 1988; Emmanuel & Berkowitz 2005; Noiriel *et al.* 2009). In the case of a two-dimensional REV made up of a solid cylinder inside a square box ($Da_{II} < 1$), the relation between the surface area and porosity can be expressed as,

$$\frac{A_e}{A_0} = \left(\frac{1-\phi}{1-\phi_0}\right)^{1/2}. \tag{4.2}$$

In (4.2), A_0 and ϕ_0 correspond to the initial surface area and porosity, respectively. Surprisingly, this relation holds even when the solid pillar deviates from the cylindrical shape. Nevertheless, one has to be careful with the extrapolation of this relationship to more complex situations. For example, if the relationship of (4.2) is still valid for a 3-D porous medium made of cylinders, the exponent is 3/2 instead of 1/2 if the medium is made by a package of spherical grains. More complex models have also been proposed in the literature like the sugar lump model proposed by Noiriel *et al.* (2009) that assumes that the dissolution process dissociates the particles that composed the medium, which causes a significant increase in the surface area.

The permeability–porosity relation can be obtained by upscaling the pore-scale simulation results. For a given flow condition, i.e. *Pé* and Da_{II}, the evolution of the permeability in the fifth REV is obtained by volume averaging the velocity profile

https://doi.org/10.1017/jfm.2017.499 Published online by Cambridge University Press

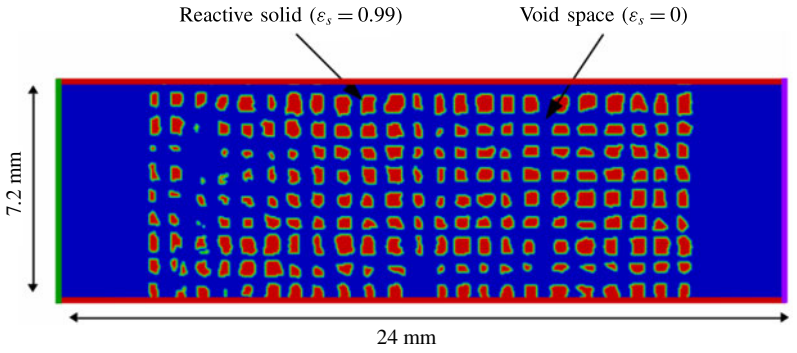


FIGURE 14. (Colour online) Schematic of the two-dimensional porous medium. Blue corresponds to the void space ($\varepsilon_f = 1$) and red to the solid ($\varepsilon_f = 0.01$).

and pressure gradient and inverting Darcy's law at every time step. Correlations to relate permeability and porosity in the form,

$$\frac{K}{K_0} = \left(\frac{\phi}{\phi_0}\right)^p \left(\frac{1-\phi}{1-\phi_0}\right)^{-q}, \tag{4.3}$$

are sought, where K_0 and ϕ_0 are the initial permeability and initial porosity. For all the simulations regardless of the dissolution regime, we obtain $p = 3 \pm 5\,\%$ and $q = 2 \pm 5\,\%$ by nonlinear regression.

4.2. *Emergence of dissolution wormholes*

We now consider the dissolution of a more complex pore space and we discuss the emergence of wormholes based on the flow conditions. The simulation set-up, i.e. geometry, fluid and rock properties, is based on the work of Song *et al.* (2014) who conducted dissolution experiments in a real rock micro-model directly etched in a carbonate. It consists of multiple solid pillars, approximately 500 μm $\times$ 500 μm, distributed uniformly in a 24 mm $\times$ 7.2 mm two-dimensional domain. The pillars are aligned and separated from each other by 300 μm wide vertical and horizontal channels, as illustrated in figure 14. The porosity, permeability and specific area of the domain are estimated numerically to be $\phi_0 \approx 0.76$, $K_0 = 1.3 \times 10^{-8}$ m^2 and $A_0 = 2310$ m^{-1}, respectively. The computational domain is meshed using a 500 $\times$ 150 Cartesian grid. The top and bottom boundaries are set as impermeable walls, i.e. no-slip boundary conditions. One per cent of acid is injected from the left-hand side of the domain at a constant velocity $v_0 = 10^{-3}$ m s^{-1} corresponding to $Re \approx 0.1$. The right-hand side is an outflow condition. Simulation properties are set to $\mu_f = 10^{-3}$ Pa s, $\rho_f = 1000$ kg m^{-3}, $\rho_s = 2165$ kg m^{-3}, $\beta = 1$ and $k_0 = 10^{-15}$ m^2.

We performed multiple simulations with different reaction rates at the solid surface, ranging from $r = 10^{-5}$ m s^{-1} to $r = 10^{-1}$ m s^{-1}, and different diffusivity coefficients ranging from $D_A = 10^{-10}$ m^2 s^{-1} to $D_A = 10^{-5}$ m^2 s^{-1}. Similar to Song *et al.* (2014) experiments, the acid is injected for 45 min. The time step was set to $\Delta t = 10^{-3}$ s. The simulations were performed on eight cores at the Stanford Center for Computational Earth and Environmental Sciences.

In line with other observations (Daccord, Lietard & Lenormand 1993; Fredd & Fogler 1998*a*,*b*; Golfier *et al.* 2002; Szymczak & Ladd 2009), the pore space

https://doi.org/10.1017/jfm.2017.499 Published online by Cambridge University Press

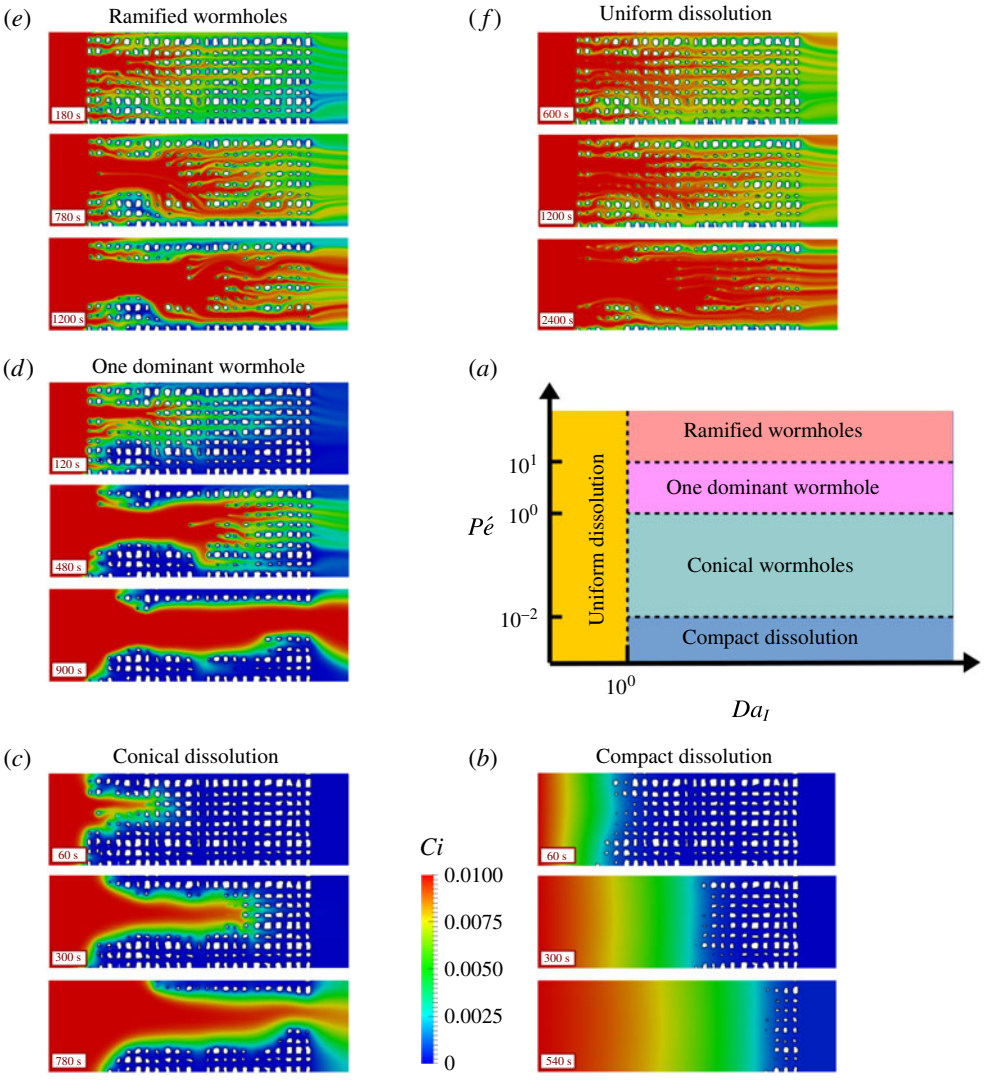


FIGURE 15. (Colour online) Prediction of the evolution of the pore space of a micro-model for different values of the constant of reaction and of the diffusion coefficient.

structure after dissolution is significantly different according to the injection rate and the mineral reactivity. The simulation results exhibit five different dissolution patterns: (*b*) compact or facial dissolution, (*c*) conical wormhole, (*d*) one dominant wormhole, (*e*) ramified wormholes and (*f*) uniform dissolution. The *Pé*–Da_I diagram (figure 15*a*) summarizes the different regimes obtained numerically according to the Péclet and the Damköhler numbers. The general features of the regime diagram agree well with the results of Golfier *et al.* (2002) and Szymczak & Ladd (2009). The transitions between the different regimes, however, differ from these studies. Several reasons can explain these discrepancies. First the characteristic lengths used to compute the Péclet and Damköhler numbers are not the same. In particular, the Péclet number (2.16) is evaluated from the square root of the permeability of the domain, $\sqrt{K}$, and the second

https://doi.org/10.1017/jfm.2017.499 Published online by Cambridge University Press

Damköhler number, Da_{II}, from the specific surface area, A_e^{-1} (2.17). Hence, the first Damköhler number, Da_I, used to build the phase diagrams in Golfier *et al.* (2002) and Szymczak & Ladd (2009) is, in our study, weighted by $(\sqrt{K}A_e)^{-1}$ (2.18). Second, the simulations of Golfier *et al.* (2002) are based on a hybrid scale formulation that involves heuristic approximations for the permeability–porosity relationship and the dissolution rate in the block matrix while our simulation framework solves the directly physics at the pore scale.

For very small Péclet numbers ($Pé \leqslant 10^{-2}$) and $Da_I > 1$, the concentration profile and the dissolution front are very stable as shown in figure 15(*b*). In this regime, usually qualified as compact, or facial dissolution, the flow is very slow, and the acid is transported to the mineral surface by diffusion only. For large values of the Damköhler number ($Da_I > 1$), the reaction is initiated as soon as the acid reaches the mineral surface. Because the consumption of acid at the pillars surface is fast, the progression of the acid in the domain is slowed down, which favours the dissolution of the pillars closer to the inlet. Moreover, because diffusion is the dominant mechanism for transport in the pore space, the concentration profile is homogeneous along the vertical cross-sections. When the acid reaches a row of solid grains, all the mineral is consumed before the concentration front propagates to the next row. Macroscopically, the average dissolution rate is linear (see figure 16*a*) until all the grains are dissolved.

For $Da_I > 1$ and larger injection rates, but still in a diffusion-dominated transport regime ($1 \geqslant Pé > 10^{-2}$), the dissolution front is no longer uniform along the vertical cross-sections, and a faster region drags the dissolution front with it forming a conical pattern (figure 15*c*). The acid penetrates into the matrix surrounding the conical wormhole mainly by diffusion. This leads to different characteristic times for the average dissolution rate, as illustrated in figure 16(*a*): in the early times of the dissolution process, the average rate of reaction is linear, and once the conical wormhole reaches the outlet of the domain, the slope is smoother because the diffusion is the dominant mechanism that brings acid at the surface of the grains surrounding the wormhole.

For $Da_I > 1$ and $10 \geqslant Pé > 1$, we observe one dominant wormhole (figure 15*d*). In this dissolution regime, the transport mechanism of acid in the void space is dominated by advection. Because the pore space heterogeneity generates important spatial variations in the velocity profile, the acid penetrates into the domain according to the faster region. Once a pillar disappears, it creates a pathway through which the acid flows preferentially. Moreover, diffusion is weak compared with advection; therefore, the transport of the acid from the wormhole to the matrix is limited to the grains surrounding the wormhole with the consequence of an aperture increase. Macroscopically, these dissolution mechanisms are described by two different slopes for the average dissolution rate (figure 16*a*). Before the wormhole reaches the right-hand side of the domain, the slope is steep showing that the reaction of acid at the grain surface is fast. After breakthrough, the slope is less steep because smaller amounts of acid reach the solid grains in the matrix. This second part of the dissolution process will be a plateau if the matrix permeability is small compared with the wormhole aperture.

For $Da_I > 1$ and $Pé > 10$ the dissolution pattern is made up of ramified wormholes (figure 15*e*). In this regime, advection is the strongest transport mechanism, and bifurcations of the local flow generate multiple dissolution pathways. The average dissolution exhibits two different slopes, but the transition between the two is less abrupt compared with the case of a single dominant wormhole.

https://doi.org/10.1017/jfm.2017.499 Published online by Cambridge University Press

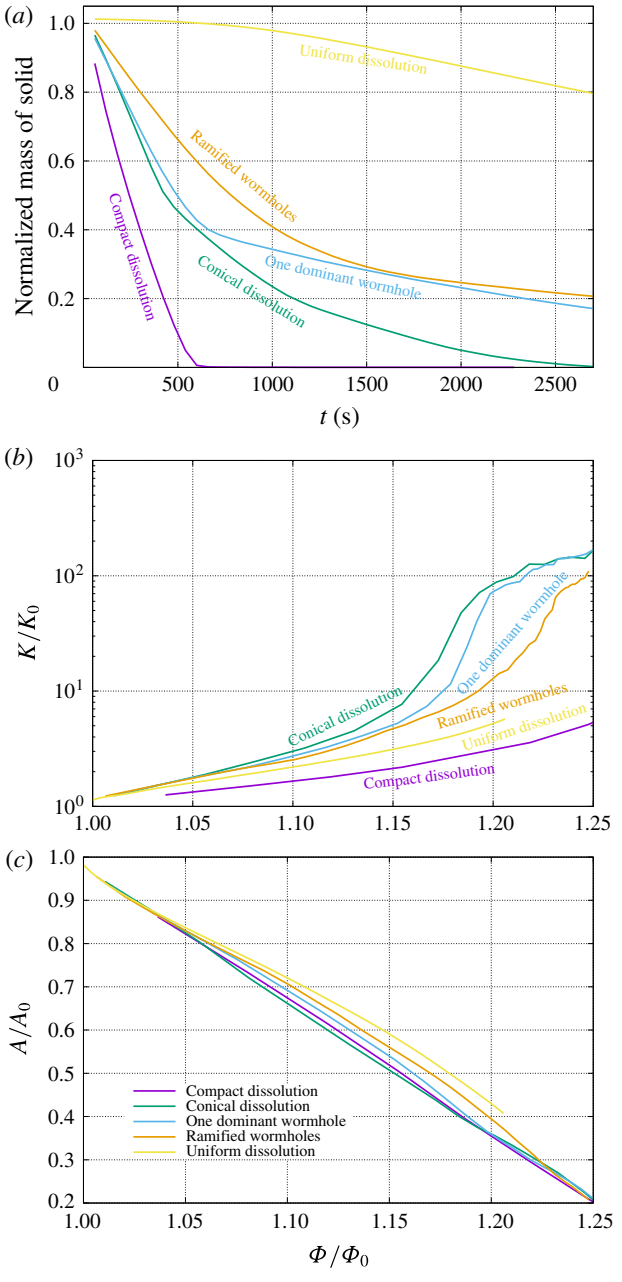


FIGURE 16. (Colour online) Plots of the average properties under different flow conditions. (*a*) Evolution of the mass of solid normalized by the initial mass, (*b*) permeability–porosity relationships, (*c*) specific area–porosity relationships.

Finally, for very small Damköhler number ($Da_I \leqslant 1$) and regardless of the Péclet number, the dissolution of the grains is uniform (figure 15*f*). In this regime, the characteristic time scale for the chemical reaction is longer than the transport time scale. Hence, the acid penetrates by convection and diffusion into the domain and contaminates almost the entire pore space. The acid at the solid surface is consumed

https://doi.org/10.1017/jfm.2017.499 Published online by Cambridge University Press

at a smaller rate than the renewal rate leading to a homogeneous dissolution pattern. Compared with the other dissolution regimes, we see in figure 16(*a*) that for small Damköhler number the total rate of dissolution starts slow and then accelerates, while for larger Da_I, it slows down during the process.

In addition to the evolution of the total mass of solid in the domain during the dissolution process, we also plot in figure 16 the permeability–porosity and the specific area–porosity relationships for the five different dissolution regimes. We observe nonlinear variations of the permeability–porosity according to the flow conditions. The variations are more important for regimes involving large wormholes, such as conical dissolution, or a single dominant wormhole. In these regimes, as soon as a wormhole reaches the domain outlet, the injected fluid flows preferentially along the new pathway created by the wormhole, which explains the large variations of the permeability. The flow resistance is then controlled by the aperture of the wormhole at the vicinity of the outlet. In the case of ramified wormholes, multiple preferential pathways percolate, and the variation although still important is smoother. For the compact and uniform dissolution regimes, there are no large channels to favour the flow from the inlet to the outlet, and the flow is limited by the porous medium pore throats. Figure 16(*c*) shows that the specific area–porosity relationship does not vary noticeably with the dissolution regimes.

5. Conclusion

We proposed a micro-continuum formulation based on the Darcy–Brinkman–Stokes equation to simulate dissolution phenomena at the pore scale. The results are in good agreement with the experiment of a calcite crystal dissolving in a micro-channel. The evolution of the mass of calcite in the system is well captured by the model. In particular, the petal-like shape of the grain during the dissolution process due to the hydrodynamic effects is obtained with great accuracy. We also successfully compared the simulation results with ALE simulations, which validates the DBS approach at the pore scale, in which the reactive boundary condition at the fluid/solid interface is formulated as a body force. These validation tests give significant confidence in using this framework to investigate the upscaling of rock dissolution.

We then solve the dissolution problem in a model porous medium made of an array of reactive cylinders under various flow conditions. Four different dissolution regimes have been identified from these simulations. First, for small Damköhler numbers ($Da_{II} < 1$), the local dissolution rate is homogeneous all around the grains, and the calcite size decreases consistent with an affine transformation with uniform scaling. For intermediate Damköhler numbers ($1 \leqslant Da_{II} < 10^4$), the shape of the solid is impacted by the hydrodynamics, because the local dissolution rates upstream and downstream of the cylinder are different. As a result, the grain deviates from cylindrical geometry. In this range of parameters, we identify two different regimes based on the Péclet number. For large Péclet number ($Pé > 10$), the shape is quasi-angular while the calcite edge is smoother for small Péclet number ($Pé \leqslant 10$). Macroscopically, these different regimes are described using the average dissolution rate with different values for the correction factor which reduces the available reactive surface area due to flow conditions. Based on the simulation results, we propose a simple correlation to relate the correction factor to the Péclet and Damköhler numbers.

The DBS framework is then used to investigate the dissolution of micro-model pore networks. Five different dissolution regimes are observed according to the constant of reaction at the mineral surface and the injection mass flow rate. These regimes

https://doi.org/10.1017/jfm.2017.499 Published online by Cambridge University Press

are: compact dissolution ($Pé \leqslant 10^{-2}$ and $Da_I > 1$), conical dissolution ($1 \geqslant Pé > 10^{-2}$ and $Da_I > 1$), dominant wormhole ($10 \geqslant Pé > 1$ and $Da_I > 1$), ramified wormholes ($Pé > 10$ and $Da_I > 1$) and uniform dissolution ($Da_I \leqslant 1$ and regardless the Péclet number). Permeability–porosity relationships are obtained by upscaling the pore-scale simulation results, and we show that the permeability variations are nonlinear with the injection mass flow rate.

The DBS formulation offers new possibilities to obtain reference solutions of dissolution phenomena at the pore scale and gain new insights regarding the larger-scale behaviour. In particular, the DBS formulation can be used to predict permeability–porosity relationships that can be used in Darcy-scale reservoir simulators.

Acknowledgements

We acknowledge the Office of Basic Energy Sciences Energy Frontier Research Center under Contract number DE-AC02-05CH11231 and the TOTAL STEMS project for financial support. We thank the Stanford Center for Computational Earth and Environmental Sciences (CEES) for computational support. We also acknowledge W. Song for her participation in the design of the microfluidic device.

REFERENCES

ALGIVE, L., BEKRI, S. & VIZIKA, O. 2010 Pore-network modeling dedicated to the determination of the petrophysical-property changes in the presence of reactive fluid. *SPE J.* **15** (03), 618–633.

ANGOT, P., BRUNEAU, C.-H. & FABRIE, P. 1999 A penalization method to take into account obstacles in incompressible viscous flows. *Numer. Math.* **81** (4), 497–520.

BÉKRI, S., THOVERT, J. F. & ADLER, P. M. 1995 Dissolution of porous media. *Chem. Engng Sci.* **50** (17), 2765–2791.

BOUSQUET-MELOU, P., GOYEAU, B., QUINTARD, M., FICHOT, F. & GOBIN, D. 2002 Average momentum equation for interdendritic flow in a solidifying columnar mushy zone. *Intl J. Heat Mass Transfer* **45** (17), 3651–3665.

BRINKMAN, H. C. 1947 A calculation of the viscous force exerted by a flowing fluid on a dense swarm of particles. *Appl. Sci. Res.* **A1**, 27–34.

CHEN, L., KANG, Q., VISWANATHAN, H. S. & TAO, W.-Q. 2014 Pore-scale study of dissolution-induced changes in hydrologic properties of rocks with binary minerals. *Water Resour. Res.* **50** (12), 9343–9365.

COHEN, C. E., DING, D., QUINTARD, M. & BAZIN, B. 2008 From pore scale to wellbore scale: impact of geometry on wormhole growth in carbonate acidization. *Chem. Engng Sci.* **63** (12), 3088–3099.

COHEN, Y. & ROTHMAN, D. H. 2015 Mechanisms for mechanical trapping of geologically sequestered carbon dioxide. *Proc. R. Soc. Lond.* A **471**, 20140853.

DACCORD, G. & LENORMAND, R. 1987 Fractal patterns from chemical dissolution. *Nature* **325** (6099), 41–43.

DACCORD, G., LIETARD, O. & LENORMAND, R. 1993 Chemical dissolution of a porous medium by a reactive fluid – ii. Convection versus reaction, behavior diagram. *Chem. Engng Sci.* **48** (1), 179–186.

DAVARZANI, H., MARCOUX, M. & QUINTARD, M. 2010 Theoretical predictions of the effective thermodiffusion coefficients in porous media. *Intl J. Heat Mass Transfer* **53** (7), 1514–1528.

EDWARDS, D. A., SHAPIRO, M. & BRENNER, H. 1993 Dispersion and reaction in two-dimensional model porous media. *Phys. Fluids* A **5** (4), 837–848.

EMMANUEL, S. & BERKOWITZ, B. 2005 Mixing-induced precipitation and porosity evolution in porous media. *Adv. Water Resour.* **28** (4), 337–344.

https://doi.org/10.1017/jfm.2017.499 Published online by Cambridge University Press

FREDD, C. N. & FOGLER, H. S. 1998*a* Alternative stimulation fluids and their impact on carbonate acidizing. *SPE J.* **13** (1), 34–41.

FREDD, C. N. & FOGLER, H. S. 1998*b* Influence of transport and reaction on wormhole formation in porous media. *AIChE J.* **44** (9), 1933–1949.

GOLFIER, F., ZARCONE, C., BAZIN, B., LENORMAND, R., LASSEUX, D. & QUINTARD, M. 2002 On the ability of a Darcy-scale model to capture wormhole formation during the dissolution of a porous medium. *J. Fluid Mech.* **457**, 213–254.

GUO, J., LAOUAFA, F. & QUINTARD, M. 2016*a* A theoretical and numerical framework for modeling gypsum cavity dissolution. *Int. J. Numer. Anal. Meth. Geomech.* **40**, 1662–1689.

GUO, J., QUINTARD, M. & LAOUAFA, F. 2015 Dispersion in porous media with heterogeneous nonlinear reactions. *Trans. Porous Med.* **109** (3), 541–570.

GUO, J., VERAN-TISSOIRES, S. & QUINTARD, M. 2016*b* Effective surface and boundary conditions for heterogeneous surfaces with mixed boundary conditions. *J. Comput. Phys.* **305**, 942–963.

HSU, C. T. & CHENG, P. 1990 Thermal dispersion in a porous medium. *Intl J. Heat Mass Transfer* **33** (8), 1587–1597.

HUANG, H. & LI, X. 2011 Pore-scale simulation of coupled reactive transport and dissolution in fractures and porous media using the level set interface tracking method. *J. Nanjing University (Natural Sciences)* **47** (3), 235–251.

HUBER, C., SHAFEI, B. & PARMIGIANI, A. 2014 A new pore-scale model for linear and non-linear heterogeneous dissolution and precipitation. *Geochim. Cosmochim. Acta* **124** (0), 109–130.

ISSA, R. I. 1985 Solution of the implicitly discretised fluid flow equations by operator-splitting. *J. Comput. Phys.* **62**, 40–65.

KALIA, N. & BALAKOTAIAH, V. 2007 Modeling and analysis of wormhole formation in reactive dissolution of carbonate rocks. *Chem. Engng Sci.* **62**, 919–928.

KANG, Q., CHEN, L., VALOCCHI, A. J. & VISWANATHAN, H. S. 2014 Pore-scale study of dissolution-induced changes in permeability and porosity of porous media. *J. Hydrol.* **517**, 1049–1055.

KANG, Q., ZHANG, D. & CHEN, S. 2003 Simulation of dissolution and precipitation in porous media. *J. Geophys. Res.* **108** (B10), 1–5.

KHADRA, K., ANGOT, P., PARNEIX, S. & CALTAGIRONE, J.-P. 2000 Fictitious domain approach for numerical modelling of Navier–Stokes equations. *Intl J. Numer. Meth. Fluids* **34** (8), 651–684.

KIM, D., PETERS, C. A. & LINDQUIST, W. B. 2011 Upscaling geochemical reaction rates accompanying acidic CO_2-saturated brine flow in sandstone aquifers. *Water Resour. Res.* **47** (1), W01505.

LANDROT, G., AJO-FRANKLIN, J. B., YANG, L., CABRINI, S. & STEEFEL, C. I. 2012 Measurement of accessible reactive surface area in a sandstone, with application to CO_2 mineralization. *Chem. Geol.* **318**, 113–125.

LI, L., PETERS, C. A. & CELIA, M. A. 2006 Upscaling geochemical reaction rates using pore-scale network modeling. *Adv. Water Resour.* **29** (9), 1351–1370.

LI, X., HUANG, H. & MEAKIN, P. 2010 A three-dimensional level set simulation of coupled reactive transport and precipitation/dissolution. *Intl J. Heat Mass Transfer* **53** (13), 2908–2923.

LICHTNER, P. C. 1988 The quasi-stationary state approximation to coupled mass transport and fluid–rock interaction in a porous medium. *Geochim. Cosmochim. Acta* **52** (1), 143–165.

LIU, X., ORMOND, A., BARTKO, K., YING, L. & ORTOLEVA, P. 1997 A geochemical reaction-transport simulator for matrix acidizing analysis and design. *J. Petrol. Sci. Engng* **17** (1), 181–196.

LIU, X. & ORTOLEVA, P. 1996 A general-purpose, geochemical reservoir simulator. In *SPE Annual Technical Conference and Exhibition*, Society of Petroleum Engineers.

LUO, H., LAOUAFA, F., DEBENEST, G. & QUINTARD, M. 2015 Large scale cavity dissolution: from the physical problem to its numerical solution. *Eur. J. Mech. (B/Fluids)* **52**, 131–146.

LUO, H., LAOUAFA, F., GUO, J. & QUINTARD, M. 2014 Numerical modeling of three-phase dissolution of underground cavities using a diffuse interface model. *Intl J. Numer. Anal. Meth. Geomech.* **38**, 1600–1616.

https://doi.org/10.1017/jfm.2017.499 Published online by Cambridge University Press

LUO, H., QUINTARD, M., DEBENEST, G. & LAOUAFA, F. 2012 Properties of a diffuse interface model based on a porous medium theory for solid–liquid dissolution problems. *Comput. Geosci.* **16** (4), 913–932.

MAURI, R. 1991 Dispersion, convection, and reaction in porous media. *Phys. Fluids* A **3** (5), 743–756.

MOLINS, S., TREBOTICH, D., YANG, L., AJO-FRANKLIN, J. B., LIGOCKI, T. J., SHEN, C. & STEEFEL, C. I. 2014 Pore-scale controls on calcite dissolution rates from flow-through laboratory and numerical experiments. *Environ. Sci. Technol.* **48** (13), 7453–7460.

NEALE, G. & NADER, W. 1974 Practical significance of Brinkman's extension of Darcy's law: coupled parallel flows within a channel and a bounding porous medium. *Can. J. Chem. Engng* **52** (4), 475–478.

NOIRIEL, C., LUQUOT, L., MADÉ, B., RAIMBAULT, L., GOUZE, P. & VAN DER LEE, J. 2009 Changes in reactive surface area during limestone dissolution: an experimental and modelling study. *Chem. Geol.* **265** (1–2), 160–170; CO_2 geological storage: integrating geochemical, hydrodynamical, mechanical and biological processes from the pore to the reservoir scale.

NOIRIEL, C., MADÉ, B. & GOUZE, P. 2007 Impact of coating development on the hydraulic and transport properties in argillaceous limestone fracture. *Water Resour. Res.* **43** (9), 1–16.

OLTÉAN, C., GOLFIER, F. & BUÈS, M. A. 2013 Numerical and experimental investigation of buoyancy-driven dissolution in vertical fracture. *J. Geophys. Res.* **118** (5), 2038–2048.

ORMOND, A. & ORTOLEVA, P. 2000 Numerical modeling of reaction-induced cavities in a porous rock. *J. Geophys. Res.* **105** (B7), 16737–16747.

PANGA, M. K. R., ZIAUDDIN, M. & BALAKOTAIAH, V. 2005 Two-scale continuum model for simulation of wormholes in carbonate acidization. *AIChE J.* **51** (12), 3231–3248.

RATHNAWEERA, T. D., RANJITH, P. G. & PERERA, M. S. A. 2016 Experimental investigation of geochemical and mineralogical effects of CO_2 sequestration on flow characteristics of reservoir rock in deep saline aquifers. *Sci. Rep.* **6**, 19362.

ROMAN, S., SOULAINE, C., ABU ALSAUD, M., KOVSCEK, A. & TCHELEPI, H. 2016 Particle velocimetry analysis of immiscible two-phase flow in micromodels. *Adv. Water Resour.* **95**, 199–211.

SCHEIBE, T. D., PERKINS, W. A., RICHMOND, M. C., MCKINLEY, M. I., ROMERO-GOMEZ, P. D. J., OOSTROM, M., WIETSMA, T. W., SERKOWSKI, J. A. & ZACHARA, J. M. 2015 Pore-scale and multiscale numerical simulation of flow and transport in a laboratory-scale column. *Water Resour. Res.* **51** (2), 1023–1035.

SHAPIRO, M. & BRENNER, H. 1988 Dispersion of a chemically reactive solute in a spatially periodic model of a porous medium. *Chem. Engng Sci.* **43** (3), 551–571.

SONG, W., DE HAAS, T. W., FADAEI, H. & SINTON, D. 2014 Chip-off-the-old-rock: the study of reservoir-relevant geological processes with real-rock micromodels. *Lab on a Chip* **14**, 4382–4390.

SOULAINE, C., GJETVAJ, F., GARING, C., ROMAN, S., RUSSIAN, A., GOUZE, P. & TCHELEPI, H. 2016 The impact of sub-resolution porosity of x-ray microtomography images on the permeability. *Trans. Porous Med.* **113** (1), 227–243.

SOULAINE, C., QUINTARD, M., ALLAIN, H., BAUDOUY, B. & WEELDEREN, R. V. 2015 A piso-like algorithm to simulate superfluid helium flow with the two-fluid model. *Comput. Phys. Commun.* **187** (0), 20–28.

SOULAINE, C. & TCHELEPI, H. A. 2016*a* Micro-continuum approach for pore-scale simulation of subsurface processes. *Trans. Porous Med.* **113**, 431–456.

SOULAINE, C. & TCHELEPI, H. A. 2016*b* Micro-continuum formulation for modelling dissolution in natural porous media. In *ECMOR XV – 15th European Conference on the Mathematics of Oil Recovery 29 August–1 September 2016, Amsterdam, Netherlands*, pp. 1–11. EAGE.

STARCHENKO, V., MARRA, C. J. & LADD, A. J. C. 2016 Three-dimensional simulations of fracture dissolution. *J. Geophys. Res. Solid Earth* **121**, 6421–6444.

STEEFEL, C. I., MOLINS, S. & TREBOTICH, D. 2013 Pore scale processes associated with subsurface CO_2 injection and sequestration. *Rev. Mineralogy Geochem.* **77** (1), 259–303.

SWOBODA-COLBERG, N. G. & DREVER, J. I. 1993 Mineral dissolution rates in plot-scale field and laboratory experiments. *Chem. Geol.* **105** (1–3), 51–69.

https://doi.org/10.1017/jfm.2017.499 Published online by Cambridge University Press

SZYMCZAK, P. & LADD, A. J. C. 2004 Microscopic simulations of fracture dissolution. *Geophys. Res. Lett.* **31** (23), 1–4.

SZYMCZAK, P. & LADD, A. J. C. 2009 Wormhole formation in dissolving fractures. *J. Geophys. Res.* **114** (B6), 1–22.

TREBOTICH, D. & GRAVES, D. 2015 An adaptive finite volume method for the incompressible Navier–Stokes equations in complex geometries. *Commun. Appl. Math. Comput. Sci.* **10** (1), 43–82.

VAFAI, K. & TIEN, C. L. 1981 Boundary and inertia effects on flow and heat transfer in porous media. *Intl J. Heat Mass Transfer* **24** (2), 195–203.

VAFAI, K. & TIEN, C. L. 1982 Boundary and inertia effects on convective mass transfer in porous media. *Intl J. Heat Mass Transfer* **25** (8), 1183–1190.

VARLOTEAUX, C., BÉKRI, S. & ADLER, P. M. 2013*a* Pore network modelling to determine the transport properties in presence of a reactive fluid: from pore to reservoir scale. *Adv. Water Resour.* **53**, 87–100.

VARLOTEAUX, C., VU, M. T., BÉKRI, S. & ADLER, P. M. 2013*b* Reactive transport in porous media: pore-network model approach compared to pore-scale model. *Phys. Rev.* E **87** (2), 023010.

WAKAO, N. & SMITH, J. M. 1962 Diffusion in catalyst pellets. *Chem. Engng Sci.* **17** (11), 825–834.

WHITAKER, S. 1999 *The Method of Volume Averaging*. Kluwer Academic.

WILLIAMS, B. B., GIDLEY, J. L. & SCHECHTER, R. S. 1979 *Acidizing Fundamentals*.; Henry L. Doherty Memorial Fund of AIME, Society of Petroleum Engineers of AIME.

XU, Z., HUANG, H., LI, X. & MEAKIN, P. 2012 Phase field and level set methods for modeling solute precipitation and/or dissolution. *Comput. Phys. Commun.* **183** (1), 15–19.

https://doi.org/10.1017/jfm.2017.499 Published online by Cambridge University Press